Acta Polytechnica **65**(4):442–453, 2025
https://doi.org/10.14311/AP.2025.65.0442

Published by the Czech Technical University in Prague

ANALYTICAL AND NUMERICAL ANALYSIS OF FILAMENT-WOUND TOROIDAL PRESSURE VESSEL LOADED BY INTERNAL PRESSURE AND TEMPERATURE FIELD

Zdeněk Padovec

Czech Technical University in Prague, Faculty of Mechanical Engineering, Department of Mechanics, Biomechanics and Mechatronics, Technická 4, 160 00 Prague, Czech Republic

correspondence: zdenek.padovec@fs.cvut.cz

Abstract. The presented work deals with the analysis of a toroidal pressure vessel manufactured using filament winding technology. An analytical model based on netting theory was used to determine the pressure vessel meridian curve, winding angle, and thickness change for two ratios of the inner and outer radius of the toroid. The theory of orthotropic continuum was used to determine the stress distribution along the meridian of the torus for loading by internal pressure and temperature field. The stress state was also analysed with the strength criteria for composite materials. The Finite Element Method (FEM) was used for the validation of the analytical model and for the determination of the filling hole effect on the stress state – the violation of membrane stress in its vicinity. The analytical model provides a fast solution, the validity of which was confirmed by FEM, that the temperature (especially after the curing process) has a non-negligible effect on the resulting failure index.

Keywords: Toroidal pressure vessel, filament winding, stress analysis, classic lamination theory, FEM.

1. Introduction

Pressure vessels, especially composite ones, are widely used in modern engineering applications due to their variability and excellent strength-to-weight ratio. The authors of previous works deal with classic integrally-wound cylindrical pressure vessels (of type IV and V [1]) with focus on end domes [2] and their optimisation [3] according to membrane stress state, while taking into account additional stresses in the cylinder/dome junction [4], and the complexity of the whole design process [5]. A torus is an axisymmetric shell of revolution created by rotating an arbitrary two-dimensional shape 360° around a central axis to form a ring-shaped structure, where the cross-sectional shape does not intersect the axis of revolution. Toroidal winding is more complex than classical cylindrical winding due to the need to feed the filaments through the central hole of the torus [6]. In toroidal winding, the mandrel rotates in a horizontal plane and its rotation is driven by friction rollers that closely contact the outer section of the mandrel. The resultant winding angle ($[\pm\omega]_n$ – symmetrically balanced layer) is dictated by the velocities of both the mandrel and the feed eye ring. The feed eye of the winding machine rotates in an intersecting plane perpendicular to the mandrel causing the fibre to always make contact with the mandrel surface at a tangent [7]. The scheme of toroidal filament winding can be seen in Figure 1. The meridian curve of the wound toroid can be obtained using the netting theory [8] and the geodesic [9] and isotensoidal conditions [10] for the possible ratios of the inner and outer toroid radius [11] with respect to technological requirements [12]. Geodesic and non-geodesic winding angles/pattern can be seen in Figure 2. The theory of orthotropic continuum [13], namely the classic lamination theory (CLT) [14], and selected strength criteria [15] can be used for obtaining the stress/strain equations for the given geometry. The toroidal construction was analysed for the loading by internal pressure, but also with the effect of uniform temperature field loading with the focus on the cooling after the curing cycle, which causes residual stresses in the construction [16]. A very similar analysis, but only applied to internal overpressure load and toroidal pressure vessel with metallic liner overwound with just hoop layers, was performed in [17]. The presented work also studies the effect of the opening (filling hole) on the stress state in its vicinity. For toroidal vessels, openings would ideally be located at or near the inner equator so that all valves, pressure regulators, and connection components can be protected from an accidental impact damage [18] but there are other possibilities where to locate them (poles, outer equator) [19]. Also, the wall of the torus is thickest at or near its inner equator [20]. FEM is a powerful tool that can be applied to many engineering problems, including the presented one [21] or the coupling between thermal and structural interaction [22]. It was used to verify the analytical solution for internal pressure and temperature loads and to determine the failure index around the filling hole.

An example of the toroidal construction efficiency is a promising gaseous fuel tank design, due to its space-saving and weight-reducing potential, its lack of structurally inefficient domed heads, and the potentially improved protection of the pressure regulator [21].

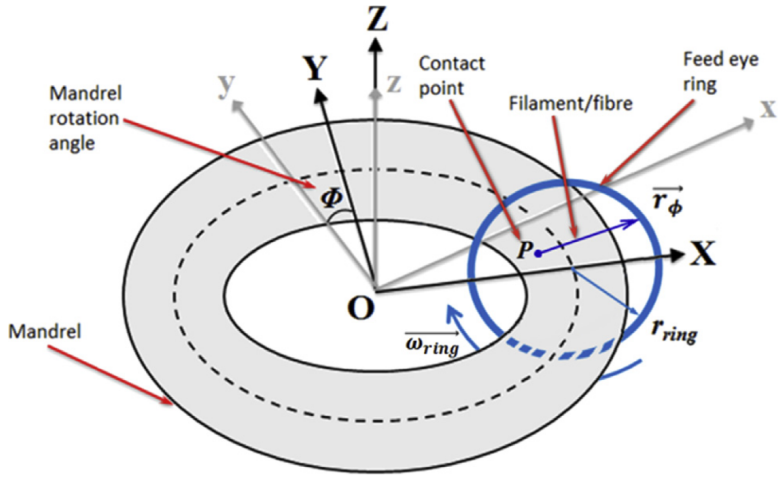

FIGURE 1. Schematic of toroidal filament winding process [7].

(A). Geodesic and non-geodesic scheme of winding.

(B). Geodesic pattern.

(C). Non-geodesic pattern.

FIGURE 2. Geodesic and non-geodesic scheme of winding [23] and geodesic and non-geodesic pattern [7].

Toroidal construction is particularly well-suited to spaces with limited height and length such as the spare tyre cavities in passenger vehicles. Cylindrical vessels that fit within available onboard spaces with length-to-width ratios ranging from approximately 1:1.5 to 1:4 [24]. Toroidal vessels are more appropriate in square spaces, as their length-to-width ratio is 1:1.

2. Materials and methods

2.1. Determination of meridian curve

The first step is to determine the meridian curve of the wound toroid, which should respect the isotensoidal and geodesic conditions [10]. The netting theory [8], which puts the membrane forces in the shell and forces in the fibres into equilibrium, was used. The solution is based on the equality of the integrals (i.e. the condition that y values for the inner and outer toroid equator must be the same – see Figure 3 for details):

$$-\int_{\omega_m}^{\omega_o} F(\omega)\, d\omega = \int_{\omega_m}^{\omega_i} F(\omega)\, d\omega, \tag{1}$$

where:

$$F(\omega) = \frac{\sin\omega_m \frac{\cos\omega}{\sin^2\omega}}{\left[\left(\frac{\sin^2\omega_m - \sin^2\omega_o}{\sin^2\omega_m - \sin^2\omega}\frac{\sin^2\omega}{\sin^2\omega_o}\frac{\cos\omega}{\cos^2\omega_o}\right)^2 - 1\right]^{\frac{1}{2}}}, \tag{2}$$

and ω_i is the winding angle on the inner radius of the toroid, ω_o is the winding angle on the outer radius of the toroid, and ω_m is the winding angle at the origin of coordinates (the pole of the torus). For a given ratio between an inner radius r_i and outer radius r_o, there is only one angle ω_m from which the geometry of the meridian of the torus can be determined. The equation for the winding angle change can be written as:

$$r_i \sin\omega_i = a\sin\omega_m = r_o \sin\omega_o, \tag{3}$$

where a is the radius passing through the origin of coordinates. With the knowledge of the winding angle, we can obtain x and y coordinates of the meridian curve written in dimensionless form, as follows:

$$\begin{aligned} \frac{y}{a} &= \pm\int_{\omega_m}^{\omega} F(\omega)\, d\omega, \\ \frac{x}{a} &= \frac{\sin\omega_m}{\sin\omega} - 1. \end{aligned} \tag{4}$$

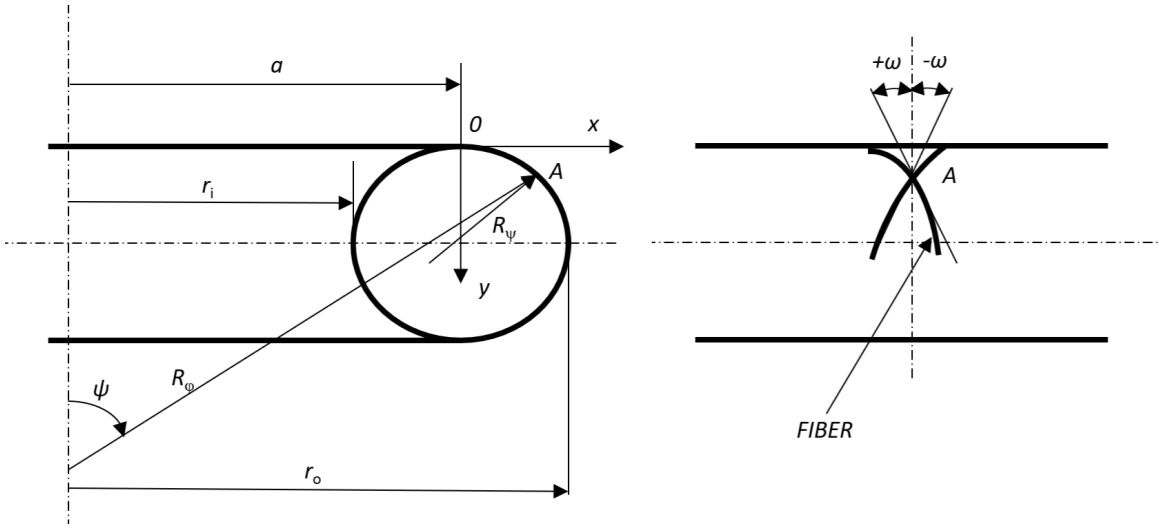

FIGURE 3. Geometry of wound toroid.

A change in the wall thickness caused by the winding of a tape of a constant width on a different radius r is typical for each shell with double curvature. The wall thickness can be calculated as [20]:

$$h = h_o \frac{r_o}{r} \frac{\cos \omega_o}{\cos \omega}, \tag{5}$$

where h_o is the thickness at the outer radius.

2.2. Thermoelastic properties of wound walls

The wall of the wound toroidal pressure vessel is made from a balanced layer (helically wound), which consists of two oriented unidirectional monolayers with winding angles + and $-\omega$. Thermoelastic properties of the wall can be calculated with the use of orthotropic continuum theory [13]. Let's consider a glass/epoxy system with thermoelastic and strength properties (according to the coordinate system in Figure 4) given in Tables 1 and 2. These values are relevant for glass/epoxy material system with a volumetric fibre content of 67 % [2].

For an oriented monolayer (see Figure 5), Duhamel-Neumann law can be written:

$$\begin{bmatrix} \sigma_\psi \\ \sigma_\varphi \\ \tau_{\psi\varphi} \end{bmatrix} = \begin{bmatrix} Q_{11} & Q_{12} & Q_{16} \\ Q_{21} & Q_{22} & Q_{26} \\ Q_{16} & Q_{26} & Q_{66} \end{bmatrix} \left\{ \begin{bmatrix} \varepsilon_\psi \\ \varepsilon_\varphi \\ \gamma_{\psi\varphi} \end{bmatrix} - \Delta T \begin{bmatrix} \alpha_\psi \\ \alpha_\varphi \\ \alpha_{\psi\varphi} \end{bmatrix} \right\}, \tag{6}$$

or:

$$\begin{bmatrix} \varepsilon_\psi \\ \varepsilon_\varphi \\ \gamma_{\psi\varphi} \end{bmatrix} = \begin{bmatrix} S_{11} & S_{12} & S_{16} \\ S_{12} & S_{22} & S_{26} \\ S_{16} & S_{26} & S_{66} \end{bmatrix} \begin{bmatrix} \sigma_\psi \\ \sigma_\varphi \\ \tau_{\psi\varphi} \end{bmatrix} + \Delta T \begin{bmatrix} \alpha_\psi \\ \alpha_\varphi \\ \alpha_{\psi\varphi} \end{bmatrix}, \tag{7}$$

where Q_{ij} are the elements of the reduced stiffness matrix and S_{ij} are the elements of the reduced compliance matrix (see [25] for details).

$$\mathbf{S}^{-1} = \mathbf{Q}. \tag{8}$$

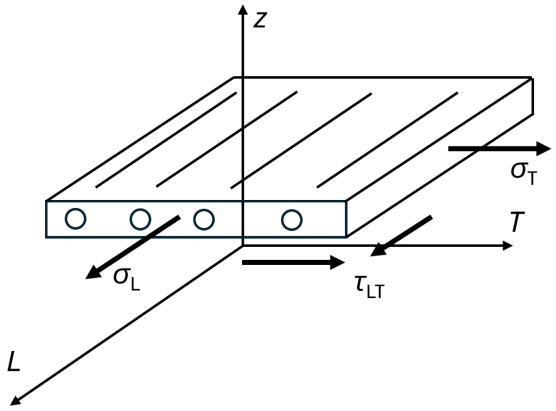

FIGURE 4. Coordinate system for unidirectional monolayer.

Elastic properties can be calculated, for example, as follows (see [25] for details):

$$S_{11} = \frac{1}{E_\psi}, \; S_{22} = \frac{1}{E_\varphi}, \ldots \tag{9}$$

Coefficients of thermal expansion (CTE's) can be written as:

$$\begin{bmatrix} \alpha_\psi \\ \alpha_\varphi \\ \alpha_{\psi\varphi} \end{bmatrix} = \begin{bmatrix} \cos^2 \omega & \sin^2 \omega \\ \sin^2 \omega & \cos^2 \omega \\ 2 \cos \omega \sin \omega & -2 \cos \omega \sin \omega \end{bmatrix} \begin{bmatrix} \alpha_L \\ \alpha_T \end{bmatrix}. \tag{10}$$

For the balanced layer (see Figure 6), which forms the torus wall, the equation can be written as:

$$\begin{bmatrix} \sigma_\psi \\ \sigma_\varphi \\ \tau_{\psi\varphi} \end{bmatrix} = \begin{bmatrix} \overline{Q_{11}} & \overline{Q_{12}} & 0 \\ \overline{Q_{12}} & \overline{Q_{22}} & 0 \\ 0 & 0 & \overline{Q_{66}} \end{bmatrix} \left\{ \begin{bmatrix} \varepsilon_\psi \\ \varepsilon_\varphi \\ \gamma_{\psi\varphi} \end{bmatrix} - \Delta T \begin{bmatrix} \overline{\alpha_\psi} \\ \overline{\alpha_\varphi} \\ 0 \end{bmatrix} \right\}, \tag{11}$$

or:

$$\begin{bmatrix} \varepsilon_\psi \\ \varepsilon_\varphi \\ \gamma_{\psi\varphi} \end{bmatrix} = \begin{bmatrix} \overline{S_{11}} & \overline{S_{12}} & 0 \\ \overline{S_{12}} & \overline{S_{22}} & 0 \\ 0 & 0 & \overline{S_{66}} \end{bmatrix} \begin{bmatrix} \sigma_\psi \\ \sigma_\varphi \\ \tau_{\psi\varphi} \end{bmatrix} + \Delta T \begin{bmatrix} \overline{\alpha_\psi} \\ \overline{\alpha_\varphi} \\ 0 \end{bmatrix}. \tag{12}$$

Material	E_L [MPa]	E_T [MPa]	G_{LT} [MPa]	υ_{LT} [-]	α_L [K^{-1}]	α_T [K^{-1}]
Glass/epoxy	48 000	17 600	8 000	0.25	6.5×10^{-6}	16.3×10^{-6}

TABLE 1. Thermoelastic properties of considered glass/epoxy material system.

Material	F_{Lt} [MPa]	F_{Lc} [MPa]	F_{Tt} [MPa]	F_{Tc} [MPa]	F_{LT} [MPa]
Glass/epoxy	1 200	600	45	145	65

TABLE 2. Strength properties of considered glass/epoxy material system. L stands for the longitudinal direction, T for the transverse direction, t for the tension, and c for the compression.

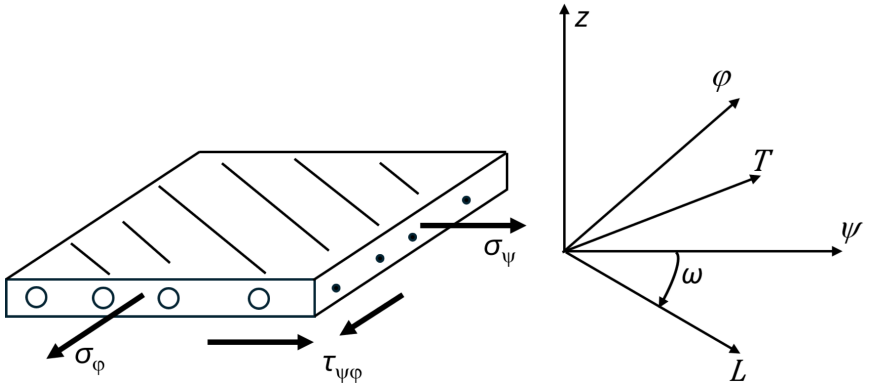

FIGURE 5. Coordinate system for oriented monolayer.

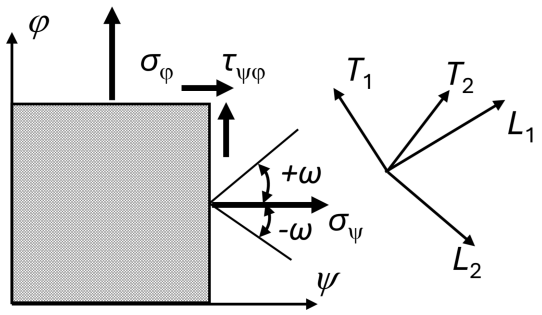

FIGURE 6. Coordinate system for balanced layer.

The interaction between the oriented monolayers during loading by normal stress caused that the resulting shear deformation is zero – $\overline{Q_{16}} = \overline{Q_{26}} = 0$. The stiffness matrix of the balanced layer is the same as the stiffness of the oriented unidirectional monolayer $\overline{Q_{ij}} = Q_{ij}$.

Elastic properties can be calculated, for example, as follows (see [25] for details):

$$\begin{aligned} \overline{E_\psi} &= \overline{Q_{11}}\left(1 - \frac{\overline{Q_{12}^2}}{\overline{Q_{11}Q_{22}}}\right), \\ \overline{E_\varphi} &= \overline{Q_{22}}\left(1 - \frac{\overline{Q_{12}^2}}{\overline{Q_{11}Q_{22}}}\right), \ldots \end{aligned} \tag{13}$$

Shear deformation of a whole balanced layer is zero, $\gamma_{\psi\varphi} = 0$, the shear stress in oriented orthotropic monolayer is:

$$\tau_{\psi\varphi} = G_{\psi\varphi}\left(-S_{61}\sigma_\psi - S_{62}\sigma_\varphi - \alpha_{\psi\varphi}\Delta T\right), \tag{14}$$

and CTE's can be written as follows:

$$\overline{\alpha_\psi} = \alpha_\psi + \alpha_{\psi\varphi} S_{61} G_{\psi\varphi},\ \overline{\alpha_\varphi} = \alpha_\varphi + \alpha_{\psi\varphi} S_{62} G_{\psi\varphi}. \tag{15}$$

A graph showing the relationship between the winding angle ω and CTE's for an oriented monolayer computed by Equation (10), and CTE's for a balanced layer computed by Equation (15), can be found in [26].

2.3. Loading by internal pressure

Loading by internal pressure (Figure 7) causes strains in the composite wall, which can be computed as follows:

$$\begin{bmatrix} \varepsilon_\psi \\ \varepsilon_\varphi \\ \gamma_{\psi\varphi} \end{bmatrix} = \begin{bmatrix} a_{11} & a_{12} & 0 \\ a_{21} & a_{22} & 0 \\ 0 & 0 & a_{66} \end{bmatrix} \begin{bmatrix} N_\psi \\ N_\varphi \\ 0 \end{bmatrix}, \tag{16}$$

where $a_{ij} = \overline{A_{ij}^{-1}}$. $\overline{A_{ij}}$ are the elements of membrane stiffness matrix, which, for balanced layer, can be computed as follows:

$$\overline{A_{ij}} = \overline{Q_{ij}} h. \tag{17}$$

Shear stress in an oriented monolayer can be computed as follows:

$$\tau_{\psi\varphi} = Q_{16}\varepsilon_\psi + Q_{26}\varepsilon_\varphi. \tag{18}$$

2.4. Loading by uniform temperature field

With respect to the assumption of thin-walled construction ($h \ll a$), the uniform distribution of temperature change ΔT, which is constant throughout the

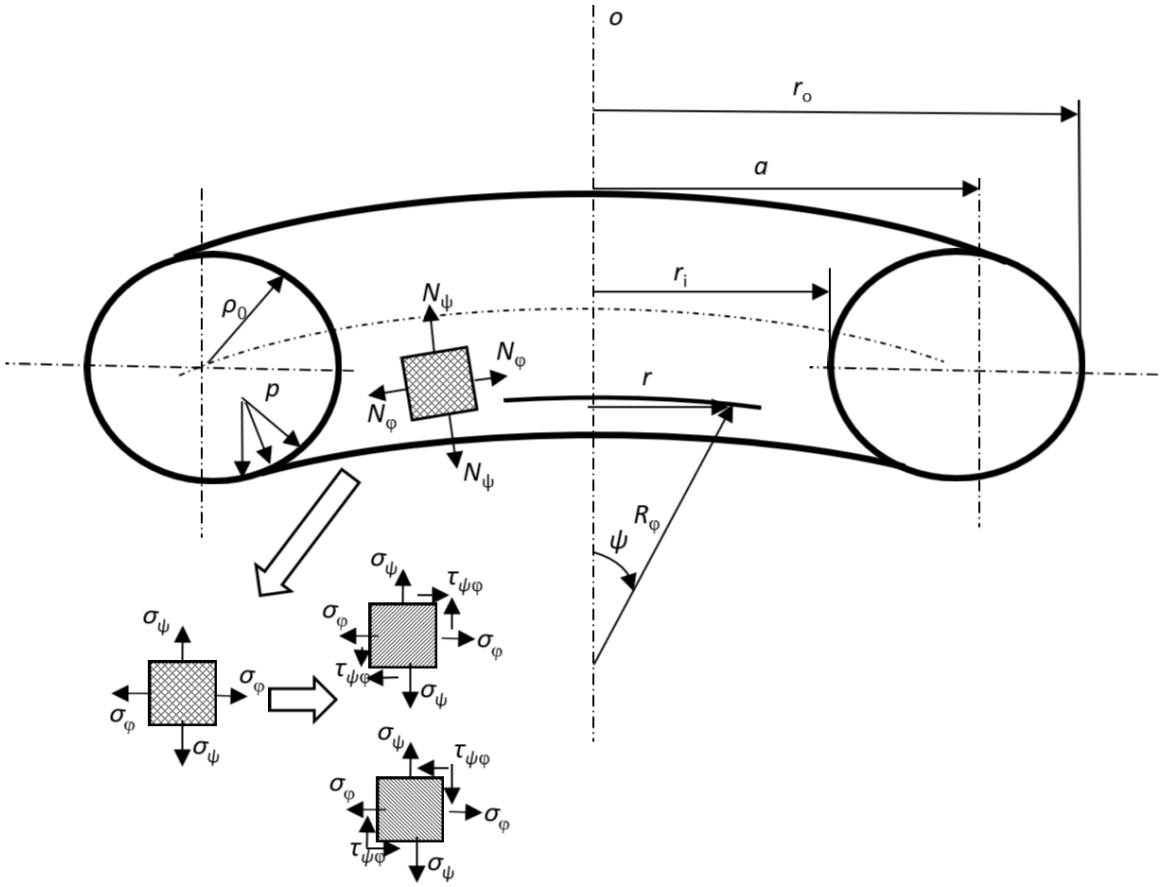

Figure 7. Toroid loaded by internal pressure.

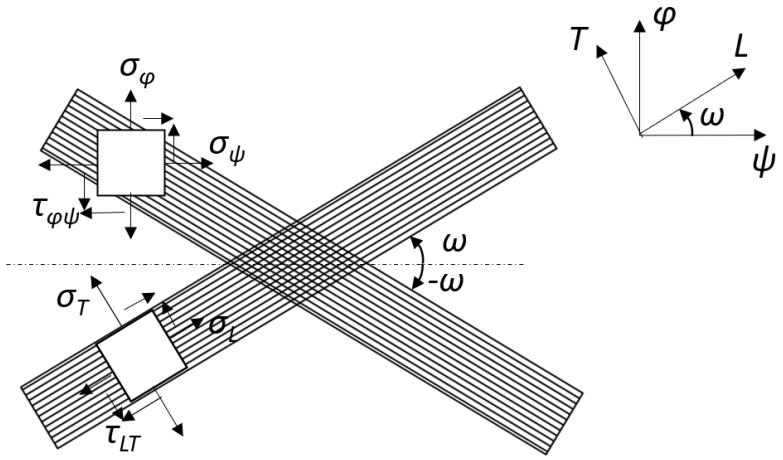

Figure 8. Stress transformation between global and local coordinate systems [2].

wall thickness, induces a constant strain distribution throughout the wall thickness. For a balanced layer, there are no normal stresses induced in the torus wall. According to this fact, Equation (14) takes the form required to describe stresses in that wall:

$$\tau_{\psi\varphi} = -\alpha_{\psi\varphi}\Delta T G_{\psi\varphi}. \tag{19}$$

2.5. Application of strength criterion

For both loading cases described in Sections 2.3 and 2.4, it is necessary to transform stresses from a global coordinate system to a local system of material orthotropy (see Figure 8):

$$\begin{bmatrix}\sigma_L\\ \sigma_T\\ \tau_{LT}\end{bmatrix} = \begin{bmatrix}\cos^2\omega & \sin^2\omega & 2\cos\omega\sin\omega\\ \sin^2\omega & \cos^2\omega & -2\cos\omega\sin\omega\\ -\cos\omega\sin\omega & \cos\omega\sin\omega & \cos^2\omega-\sin^2\omega\end{bmatrix}\begin{bmatrix}\sigma_\psi\\ \sigma_\varphi\\ \tau_{\psi\varphi}\end{bmatrix}. \tag{20}$$

Stresses, computed from Equation (20), are used as the input for the calculation of the failure index from the selected strength criterion. The maximum stress criterion was chosen (see [15] for example) and it states that failure occurs when at least one of the stresses in the material coordinates exceeds the corresponding

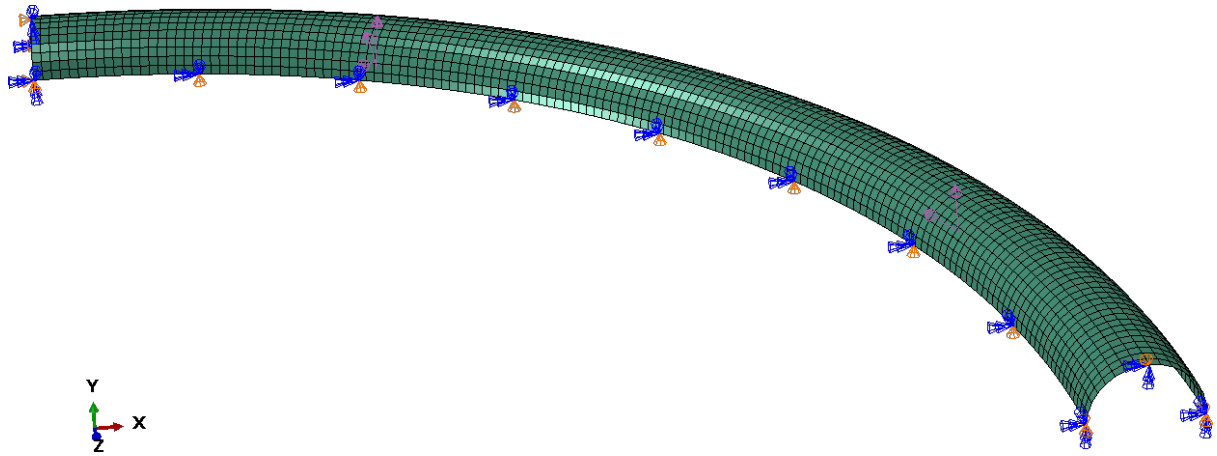

FIGURE 9. FE model of the analysed case with the use of symmetry.

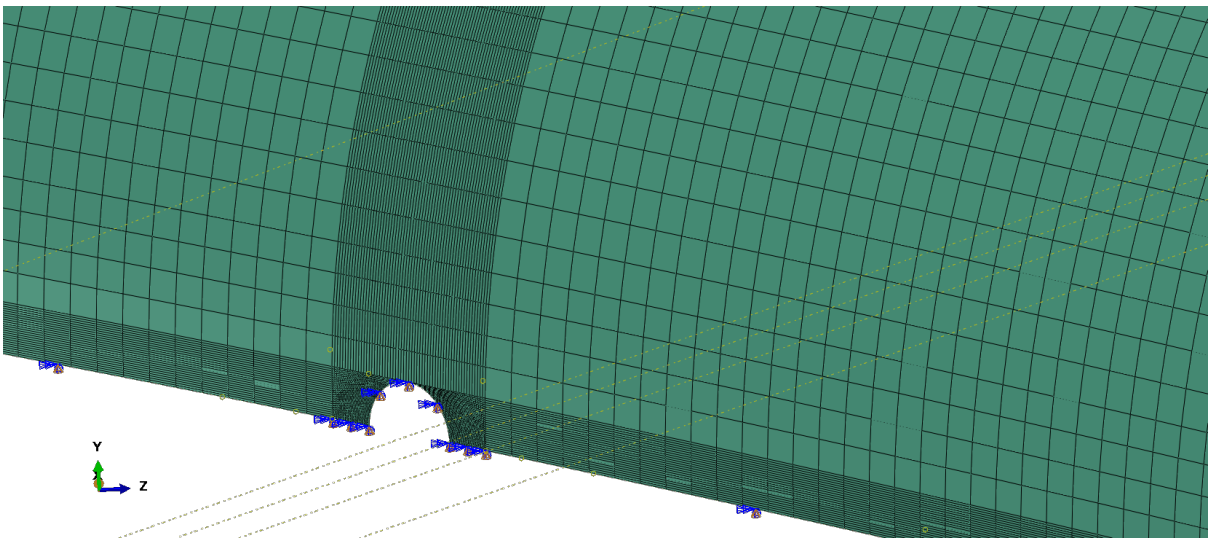

FIGURE 10. Fine mesh in filling hole's vicinity.

experimental strength value. This can be expressed as follows:

$$\begin{aligned} -F_{Lc} < \sigma_L &< F_{Lt}, \\ -F_{Tc} < \sigma_T &< F_{Tt}, \\ -F_{LT} < \sigma_{LT} &< F_{LT}. \end{aligned} \tag{21}$$

2.6. FE ANALYSIS

FE analysis was done using the commercial software Abaqus. A 1/8 of the toroid was modelled with the use of symmetry in planes xy, yz, and xz. The geometry of the toroid was cut with the use of parallels to allow for changes in wall thickness and winding angle. S4R shell elements were used for discretisation. It is a 4-node, quadrilateral, stress/displacement shell element with reduced integration and a large-strain formulation. Each node has six degrees of freedom. The linear elastic material model Lamina was used with thermoelastic and strength characteristics from Tables 1 and 2. A geometric nonlinear analysis was carried out. The FE model can be seen in Figure 9. The result of the FE analysis for both loading cases (internal pressure and uniform temperature field) is the failure index according to the maximum stress criterion.

The effect of filling the hole was analysed with the use of a similar model. A filling hole was placed on the inner equator of the toroid where the largest wall thickness and fine mesh in its vicinity was done (see Figure 10). The size of the elements was chosen after performing the mesh sensitivity test (the comparison criterion between the meshes used was the magnitude of the failure index). Each segment of the toroid with defined wall thickness and winding angle was meshed with at least three elements per arc length.

3. RESULTS AND DISCUSSION

Two ratios of $\frac{r_i}{r_o}$ were chosen for the analysis – 0.7 and 0.9. The computed meridian of the toroid compared with a circle can be seen in Figure 11. For both analysed ratios, the meridian curve can be approximated with a circle with sufficient accuracy. If the ratio of $\frac{r_i}{r_o}$ decreases, the difference between the meridian curve and the approximation with the circle increases [11]. For that case, forces from Equation (16)

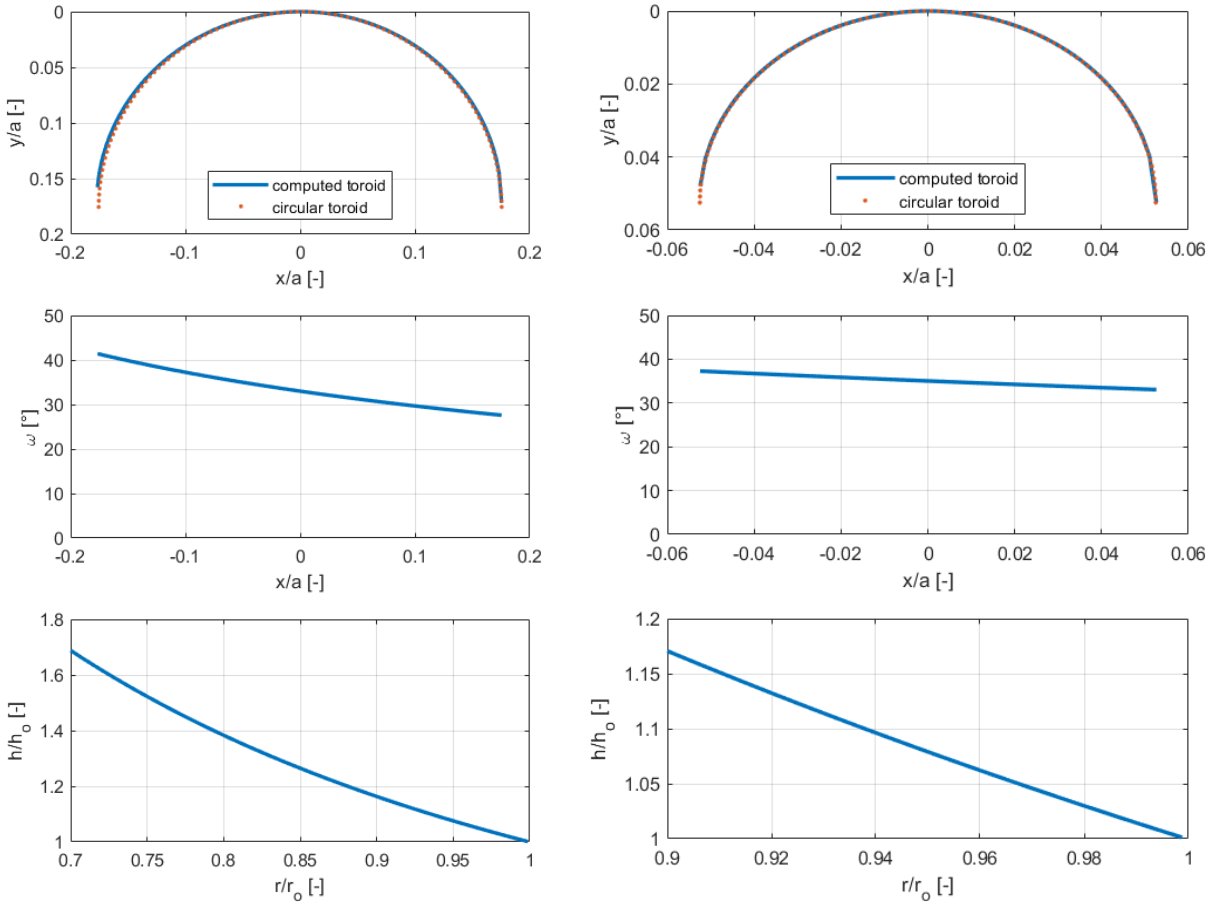

(A). $\frac{r_i}{r_o} = 0.7$. (B). $\frac{r_i}{r_o} = 0.9$.

FIGURE 11. Computed meridian of toroid compared with circle, change in winding angle ω and change in wall thickness h for $\frac{r_i}{r_o}$ ratio 0.7 and 0.9.

can be calculated as follows:

$$N_\psi = \sigma_\psi h = \frac{p\rho_0(a+r)}{2r}, \qquad N_\varphi = \sigma_\varphi h = \frac{p\rho_0}{2}, \tag{22}$$

where ρ_0 is the radius of the replacement circle that approximates the meridian of the toroid (see Figure 7).

Figure 11 also depicts the relationship between the winding angle and the position on the meridian. The winding angle is changing continuously from maximal value on inner radius r_i to minimal value on outer radius r_o. The difference between maximal and minimal values of ω decreases with the decreasing value of the ratio of radii. Figure 12 shows the relationship between the winding angle on specified positions and the ratio of radii, and it can be stated that all three angles reach the same value for the $\frac{r_i}{r_o} = 1$, which is a cylinder. For this ratio, the winding angle is $\omega = 35°\,15'$, and its complement to 90° is $54°\,75'$, which is the winding angle of the balanced layer on the cylindrical shell loaded by internal pressure [27]. As can be stated from the last part of Figure 11, the minimal thickness is on the outer equator radius and maximal on the inner equator radius. With the rising ratio of radii, the relative thickness grows the fastest.

In a global coordinate system, stress can be calculated with the use of Equations (16), (18), and (22), which can be normalised with meridional stress on the outer equator, as follows:

$$\sigma_{sr} = \sigma_{\psi o} = \frac{p\rho_0(2a+\rho_0)}{2\,(a+\rho_0)\,h}. \tag{23}$$

Figure 13 shows the relationship between the global stresses and the position on the meridian for the analysed ratios. From the graph, it can be seen that both analysed cases have normal stresses at maximum on the outer equator radius, shear stress is plotted for the positive value of winding angle $+\omega$ and has its maximum outside this area. Shear stress for the negative value of winding angle $-\omega$ has the same value but the opposite sign. These stresses were transformed according to Equation (20), and failure criterion (21) was used for the failure index evaluation. The same procedure was performed for the evaluation of temperature stresses and the failure index corresponding to the loading by uniform temperature field.

3.1. Numerical example

The numerical example was computed for toroid with $\frac{r_i}{r_o} = 0.9$. The inner radius was 450 mm and the

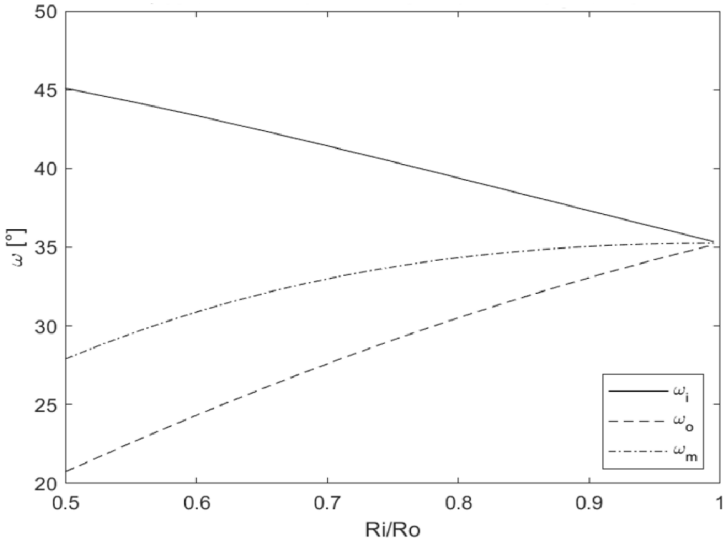

FIGURE 12. Relationship between the winding angle ω on specified positions and the ratio of radii.

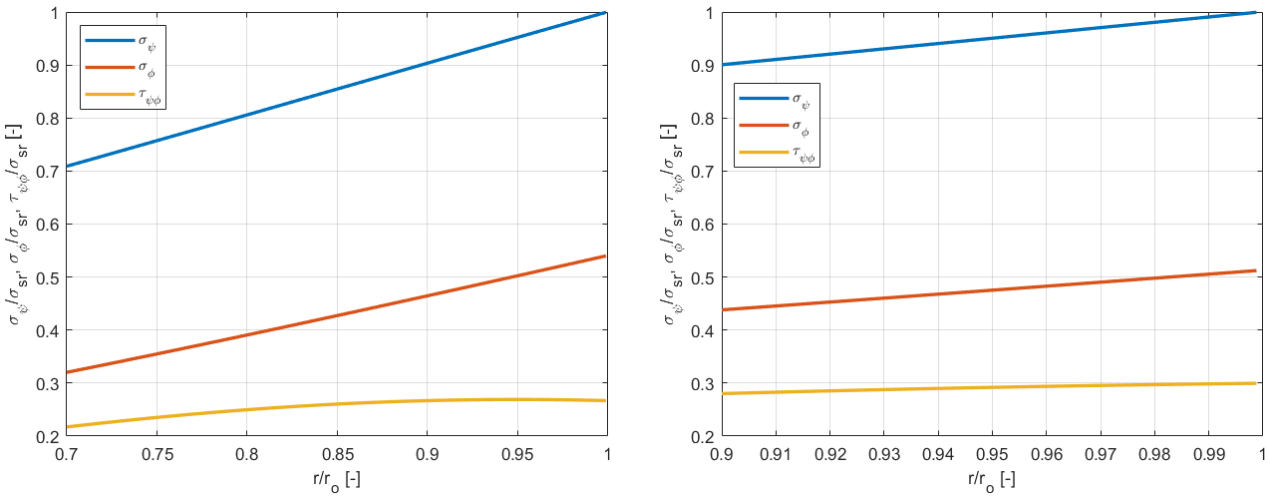

(A). $\frac{r_i}{r_o} = 0.7$. (B). $\frac{r_i}{r_o} = 0.9$.

FIGURE 13. Relationship between normal and shear stresses in global coordinate system and position on meridian for $\frac{r_i}{r_o}$ ratio 0.7 and 0.9.

outer radius was 500 mm. The wall thickness of the balanced layer at the outer radius was set to 1 mm (which means thickness of 0.5 mm for each oriented unidirectional monolayer), and the internal pressure was 3 MPa. The winding angle at the outer radius was computed from Equation (3) $\pm\omega_o = 33.05°$. The change in thickness and winding angle along the meridian, which are crucial for the computation, are taken from Figure 11b. The analysed toroid was cooled from 120 °C to 20°, which corresponds to cooling after the curing cycle of a typical epoxy resin. Also, cooling is more dangerous because σ_T has a tensile character for this material system. Margins of safety are calculated for each Equation (21), the minimum is selected, and its reciprocal value is then the desired failure index. The failure index was analytically calculated for both loading cases and compared with the results obtained by FEM. The comparison of the results is plotted in Figures 14 and 15. From the figures, it can be seen that in the case of internal pressure loading (Figure 14), the maximum failure index is at the outer equator radius and minimal at the inner one. In the case of uniform cooling (Figure 15), it is the exact opposite – the maximum failure index is at the inner equator radius and minimal at the outer one. The maximum difference between the analytical solution and the FE results is a 6 %.

The last analysed problem was the influence of the filling hole on the stress state in its vicinity. The filling hole with a diameter of 3 mm was placed at the inner equator radius, symmetrically to xz plane. The failure index around the filling hole is depicted in Figure 16 with its maximum value equal to 1.516. By comparing this value with the failure index value of 0.55 for the same area in construction without a hole (inner radius coordinate in Figure 14), it can be stated that the filling hole caused a 2.75 times greater failure index.

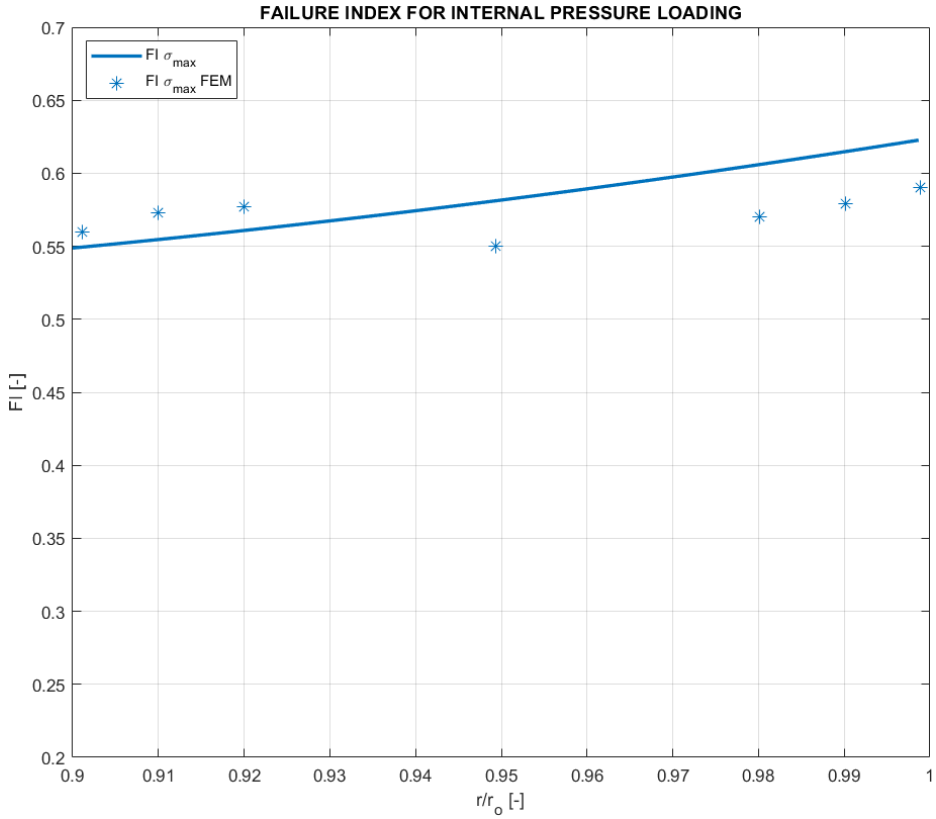

Figure 14. Comparison of failure index for internal pressure load obtained analytically and numerically, for $\frac{r_i}{r_o}$ ratio of 0.9.

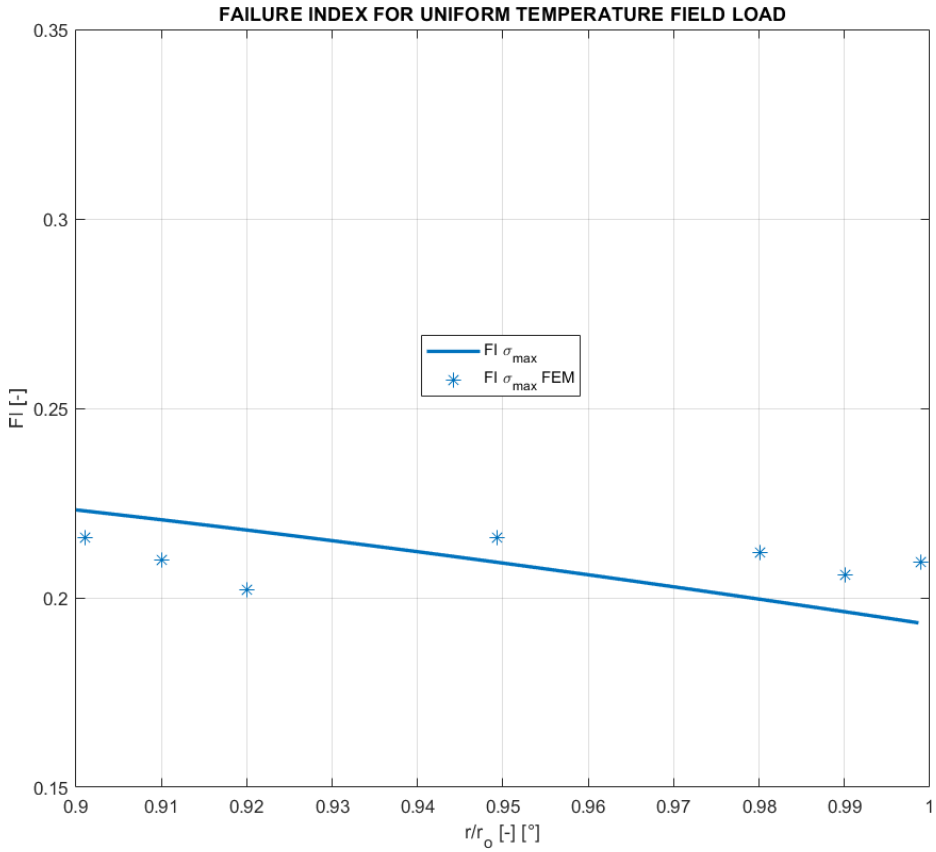

Figure 15. Comparison of failure index for uniform temperature field load obtained analytically and numerically for $\frac{r_i}{r_o}$ ratio of 0.9.

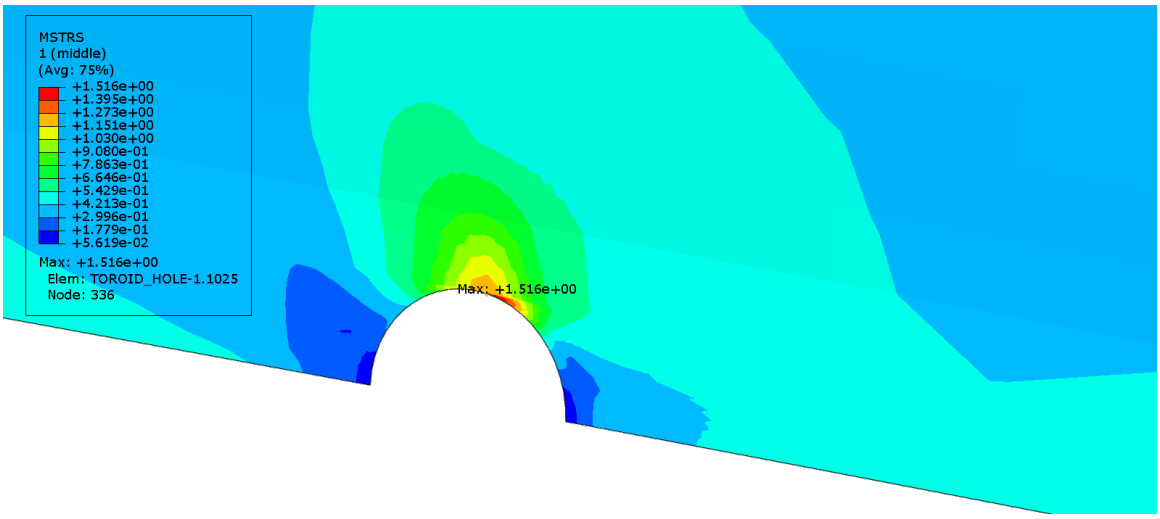

FIGURE 16. Stress concentration around filling hole expressed by failure index.

4. CONCLUSION

The analytical and numerical analysis of toroidal pressure vessel manufactured by means of filament winding was conducted for selected ratios of inner and outer equator radii. The meridian curve of the torus was investigated with the use of netting theory and geodesic condition with a conclusion that for higher ratios of radii, the meridian curve can be approximated with a circle.

Analytical and numerical solutions of the failure index along the meridian were obtained for internal pressure load and uniform cooling for the circular meridian of the torus, achieving good agreement. It can be said that the analytical solution is faster than preparing the model in FE software and it is a necessary condition for obtaining FE input data (wall thickness around the meridian, change in the winding angle). If the results from Figures 13 and 14 were superimposed together, the failure index reaches a maximum value of about 0.8. That means that the temperature influence on the resulting stresses has a non-negligible effect and it should be an indisputable part of the pressure vessel analysis. A practical implication of this fact is that if the script/program is prepared with respect to the analytical solution (Equations (16)–(18) for loading by internal pressure, Equation (19) for loading by uniform temperature field, and Equations (20) and (18) for transformation and computation of margin of safety/failure index), a fast preliminary analysis can be performed with a quick possible change of input data (inner/outer radius, internal pressure, change in temperature, material parameters, etc.) and obtain a large set of possible solutions. This large set of solutions can also be used as an input dataset for multicriteria optimisation by data-driven algorithms. The selected optimal solution should be analysed in detail with the use of FEM with a focus on structural elements that cannot be included in the analytical solution. The analytical solution can be summarised in the following points:

- Determination of the generating curve using numerical integration of Equation (2), with the use of Equation (4), and comparison with the circular approximation,
- evaluation of winding angle ω and wall thickness h along the meridian curve,
- for given internal pressure computing the force resultants in circumferential and meridional directions, membrane stiffness matrix $\overline{\mathbf{A}}$, strains and stresses in a global coordinate system in each point of the meridian curve,
- evaluation of CTE's depending on the winding angle ω in each point of the meridian curve,
- for a given temperature change, computing the stresses in a global coordinate system in each point of the meridian curve,
- transforming the stresses caused by internal pressure and temperature change from a global coordinate system to a local coordinate system, and using the chosen strength criterion to evaluate the failure index.

The numerical solution for the construction with a filling hole at the inner equator radius was done, revealing that the failure index around the hole is 2.75 times greater than in the same area of a construction without a hole. Also, the failure index for the analysed example is greater than one, which means that the construction will fail. Decreasing the failure index in this critical place can be achieved by increasing the wall thickness.

The thermoelastic properties and strengths were derived for ambient temperature, 20 °C, and in calculations, they are treated as invariants to temperature changes. In other words, the present study does not consider the viscoelastic behaviour of materials that can occur at very high temperatures, and it is not suitable for cases where material creep or cryogenic conditions are expected.

List of symbols

a Radius passing through the origin of coordinates [mm]
$\overline{\mathbf{A}}$ Membrane stiffness matrix for balanced layer [N mm]
E_L Young modulus in longitudinal direction [MPa]
E_T Young modulus in transversal direction [MPa]
F_{Lt}, F_{Lc} Strength in longitudinal direction in tension/compression [MPa]
F_{Tt}, F_{Tc} Strength in transversal direction in tension/compression [MPa]
F_{LT} Shear strength in LT plane [MPa]
G_{LT} Shear modulus in LT plane [MPa]
$G_{\psi\varphi}$ Shear modulus in $\psi\varphi$ plane [MPa]
h_o Thickness of balanced layer on outer radius [mm]
h Thickness of balanced layer on general radius [mm]
r_i Inner radius of the toroid [mm]
r_o Outer radius of the toroid [mm]
N_θ, n_ψ Force resultants in circumferential and meridional direction [$\mathrm{N\,mm^{-1}}$]
$\mathbf{Q}$ Reduced stiffness matrix for oriented monolayer [MPa]
$\overline{\mathbf{Q}}$ Reduced stiffness matrix for balanced layr [MPa]
R_θ, R_ψ Principal radii of curvature [mm]
$\mathbf{S}$ Reduced compliance matrix for oriented monolayer [$\mathrm{M\,Pa^{-1}}$]
$\overline{\mathbf{S}}$ Reduced compliance matrix for balanced layr [MPa]
ΔT Change in temperature [°C]
α_L Coefficient of thermal expansion in longitudinal direction [$\mathrm{K^{-1}}$]
α_T Coefficient of thermal expansion in transversal direction [$\mathrm{K^{-1}}$]
α_ψ Coefficient of thermal expansion in meridional direction for oriented monolayer [$\mathrm{K^{-1}}$]
α_φ Coefficient of thermal expansion in circumferential direction for oriented monolayer [$\mathrm{K^{-1}}$]
$\alpha_{\psi\varphi}$ Shear coefficient of thermal expansion in $\psi\varphi$ plane for oriented monolayer [$\mathrm{K^{-1}}$]
$\overline{\alpha_\psi}$ Coefficient of thermal expansion in meridional direction for balanced layer [$\mathrm{K^{-1}}$]
$\overline{\alpha_\varphi}$ Coefficient of thermal expansion in circumferential direction for balanced layer [$\mathrm{K^{-1}}$]
υ_{LT} Major Poisson ration in LT plane [–]
ε_ψ Strain in meridional direction [–]
ε_φ Strain in circumferential direction [–]
$\gamma_{\psi\varphi}$ Shear strain in $\psi\varphi$ plane [–]
ρ_0 Replacement circle radius that approximates the meridian of the toroid [mm]
σ_ψ Normal stress in meridional direction [MPa]
σ_φ Normal stress in circumferential direction [MPa]
σ_L Normal stress in longitudinal direction [MPa]
σ_T Normal stress in transversal direction [MPa]
$\tau_{\psi\varphi}$ Shear stress in $\psi\varphi$ plane [MPa]
τ_{LT} Shear stress in LT plane [MPa]
ω_i Winding angle on the inner radius of the toroid [°]
ω_o Winding angle on the outer radius of the toroid [°]
ω_m Winding angle on the origin of coordinates [°]
CTE Coefficient of thermal expansion
FEM Finite element method
FI Failure index

Acknowledgements

This study was supported by the Grant Agency of the Czech Technical University in Prague, under grant No. SGS24/123/OHK2/3T/12.

References

[1] International Organization for Standardization. ISO 11439:2013. Gas cylinders – High pressure cylinders for the on-board storage of natural gas as a fuel for automotive vehicles, 2013.

[2] Z. Padovec, D. Vondráček, T. Mareš. The analytical and numerical stress analysis of various domes for composite pressure vessels. *Applied and Computational Mechanics* **16**(2), 2022. https://doi.org/10.24132/acm.2022.781

[3] D. Vondráček, Z. Padovec, T. Mareš, N. Chakraborti. Optimization of dome shape for filament wound pressure vessels using data-driven evolutionary algorithms. *Materials and Manufacturing Processes* **38**(15):1899–1910, 2023. https://doi.org/10.1080/10426914.2023.2187823

[4] D. Vondráček, Z. Padovec, T. Mareš, N. Chakraborti. Analysis and optimization of junction between cylindrical part and end dome of filament wound pressure vessels using data driven evolutionary algorithms. *Proceedings of the Institution of Mechanical Engineers, Part C: Journal of Mechanical Engineering Science* **238**(6):2348–2361, 2024. https://doi.org/10.1177/09544062231191319

[5] D. Vondráček, Z. Padovec, T. Mareš, N. Chakraborti. Complex design and analysis of filament wound composite pressure vessels using data driven evolutionary algorithms. *Proceedings of the Institution of Mechanical Engineers, Part E: Journal of Process Mechanical Engineering* p. 09544089241238410, 2024. https://doi.org/10.1177/09544089241238410

[6] S. Li, J. Cook. An analysis of filament overwound toroidal pressure vessels and optimum design of such structures. *Journal of Pressure Vessel Technology* **124**(2):215–222, 2002. https://doi.org/10.1115/1.1430671

[7] L. Zu, D. Zhang, Y. Xu, D. Xiao. Integral design and simulation of composite toroidal hydrogen storage tanks. *International Journal of Hydrogen Energy* **37**(1):1027–1036, 2012. https://doi.org/10.1016/j.ijhydene.2011.03.026

[8] J. D. Marketos. Optimum toroidal pressure vessel filament wound along geodesic lines. *AIAA Journal* **1**(8):1942–1945, 1963. https://doi.org/10.2514/3.1970

[9] W. S. Read. Equilibrium shapes for pressurized fiberglas domes. *Journal of Engineering for Industry* **85**(1):115–118, 1963. https://doi.org/10.1115/1.3667557

[10] J. Zickel. Isotensoid pressure vessels. *ARS Journal* **32**:950–951, 1962.

[11] V. V. Vasiliev. *Composite pressure vessels: Design, analysis, and manufacturing*. Bull Ridge Publishing, Virginia, USA, 2009.

[12] H. Hu, S. Li, J. Wang, L. Zu. Structural design and experimental investigation on filament wound toroidal pressure vessels. *Composite Structures* **121**:114–120, 2015. https://doi.org/10.1016/j.compstruct.2014.11.023

[13] K. K. Chawla. *Composite materials: Science and engineering*. Springer, 4th edn., 2019.

[14] E. J. Barbero. *Introduction to composite materials design*. CRC Press, Florida, USA, 2nd edn., 2011. https://doi.org/10.1201/9781439894132

[15] S. Sharma. *Composite materials: Mechanics, manufacturing and modeling*. CRC Press, Florida, USA, 1st edn., 2021. https://doi.org/10.1201/9781003147756

[16] C. Liu, Y. Shi. Design optimization for filament wound cylindrical composite internal pressure vessels considering process-induced residual stresses. *Composite Structures* **235**:111755, 2020. https://doi.org/10.1016/j.compstruct.2019.111755

[17] S. Li, J. Cook. An analysis of filament overwound toroidal pressure vessels and optimum design of such structures. *Journal of Pressure Vessel Technology* **124**(2):215–222, 2002. https://doi.org/10.1115/1.1430671

[18] Y. Kisioglu. Burst pressure determination of vehicle toroidal oval cross-section LPG fuel tanks. *Journal of Pressure Vessel Technology* **133**(3):031202, 2011. https://doi.org/10.1115/1.4002863

[19] C. P. Fowler, A. C. Orifici, C. H. Wang. A review of toroidal composite pressure vessel optimisation and damage tolerant design for high pressure gaseous fuel storage. *International Journal of Hydrogen Energy* **41**(47):22067–22089, 2016. https://doi.org/10.1016/j.ijhydene.2016.10.039

[20] J. T. Hofeditz. Structural design considerations for fibrous glass pressure vessels. *Modern Plastics* **41**:127–145, 1964.

[21] M. J. Vick, K. Gramoll. Finite element study on the optimization of an orthotropic composite toroidal shell. *Journal of Pressure Vessel Technology* **134**(5):051201, 2012. https://doi.org/10.1115/1.4005873

[22] S. Sharma, C. Pany, R. Suresh, et al. Spiral wound gasket in a typical liquid engine convergent-divergent nozzle. In V. K. Singh, G. Choubey, S. Suresh (eds.), *Advances in Thermal Sciences*, pp. 187–201. Springer Nature, Singapore, 2023. https://doi.org/10.1007/978-981-19-6470-1_16

[23] L. Zu, S. Koussios, A. Beukers. Design of filament-wound circular toroidal hydrogen storage vessels based on non-geodesic fiber trajectories. *International Journal of Hydrogen Energy* **35**(2):660–670, 2010. https://doi.org/10.1016/j.ijhydene.2009.10.062

[24] H. S. Roh, T. Q. Hua, R. K. Ahluwalia. Optimization of carbon fiber usage in Type 4 hydrogen storage tanks for fuel cell automobiles. *International Journal of Hydrogen Energy* **38**(29):12795–12802, 2013. https://doi.org/10.1016/j.ijhydene.2013.07.016

[25] G. W. Ehrenstein. *Polymeric materials: Structure, properties, applications*. Carl Hanser Verlag, Germany, 2002.

[26] D. Vondráček, Z. Padovec, T. Mareš, N. Chakraborti. Analysis of thermoelastic stresses in filament wound composite pressure vessels using evolutionary deep learning and many-objective optimisation. *Philosophical Magazine Letters* **105**(1):2476499, 2025. https://doi.org/10.1080/09500839.2025.2476499

[27] D. Gay, S. V. Hoa, S. W. Tsai. *Composite materials: Design and applications*. CRC Press, Florida, USA, 1st edn., 2002. https://doi.org/10.1201/9781420031683